Applied Acoustics 105 (2016) 83–92

Contents lists available at ScienceDirect

Applied Acoustics

journal homepage: www.elsevier.com/locate/apacoust

Technical Note

A setup to study aero-acoustics for finite length ducts with time-varying shape

A. Van Hirtum *, R. Blandin, X. Pelorson

Gipsa-lab, UMR CNRS 5216, Grenoble University, France

ARTICLE INFO

Article history:
Received 14 October 2015
Received in revised form 18 November 2015
Accepted 30 November 2015

Keywords:
Controlled elastic duct deformation
Duct aero-acoustics
Dynamic replica
Physiological flow or sound production system
Upper airway

ABSTRACT

Elastic ducts with time-varying geometry are a recurrent issue in many engineering and physiological flow or sound production problems. In this study, we present and characterize a setup to study aero-acoustic phenomena through a deformable duct with time-varying geometry. The setup is designed in such a way that experimental control parameters relate directly to input parameters of a quasi-analytical geometrical model (Van Hirtum, 2015). We focus on low Mach number and moderate Reynolds number applications pertinent to physiological problems for which geometrical model input parameters can be related to well defined physiological quantities. Therefore, data gathered using the presented setup allow to study underlying physical phenomena and in addition favor comparison with high performance computational simulations as well as with analytical models for which a limited number of physiological meaningful input parameters are essential. Typical measurements illustrate the impact of geometrical control parameters on the acoustic pressure field in absence and in presence of flow, respectively.

1. Introduction

Sound production and propagation through ducts is well studied when considering ducts with a constant shape [17,4,15]. Whereas such ducts are essential for many applications – *e.g.* industry (applications related to liquid/gas transport [6,18]), musical acoustics (flute resonators or organ pipes [10]), *etc.* – much less research considers sound production and propagation through ducts with a time-varying shape. Nevertheless, physiological phenomena related to noise production and propagation often occur in ducts with a time-varying shape related to blood flow or air flow [12,5,7,8,3,2,16].

Human speech production is a common example of such a phenomenon, naturally associated with sound production, for which the duct's, *i.e.* upper airway, shape varies voluntary during articulation of different phoneme utterances [13,19,1,9]. In this case, sound through a finite duct is generated either aerodynamically somewhere in the upper airway or is due to a fluid–structure interaction resulting in auto-oscillation at the duct's inlet, *i.e.* at the larynx [9]. Obviously, the detailed geometry of a time-varying human upper airway – or more in general physiological flow or sound systems – is extremely complicated and is subject to intra- and inter-subject variability. In addition, measurement of geometrical, flow and acoustic properties on human subjects is limited and therefore not suitable for studies aiming physical understanding of sound production and propagation. Consequently, systematic physical studies often rely on simplified geometries to enhance understanding [12,9,19].

In the current work, a setup is presented to study aero-acoustics of finite ducts for moderate Reynolds numbers and low Mach numbers as suitable for physical studies of physiological flow and sound systems such as the human upper airway. It is aimed to control the duct's geometry using a limited amount of control parameters related to constriction degree, duration and position for up to two constrictions. Systematic variation of these parameters is expected to enhance model validation since most studies consider a limited amount of static geometrical configurations which hinders general conclusions [22]. In addition, new insights in transient phenomena related to controlled time-varying geometries are expected to be gained since such data are few in literature. Consequently, quantitative measurements in relation to a controlled time-varying duct geometry potentially increases understanding of the impact of the duct's geometry on the flow and sound field.

Besides possible applications related to physiological flow or sound systems the proposed setup can be used to contribute to active vibration and noise control strategies. As an example, the impact of varying the constriction degree on *e.g.* fluid–structure

* Corresponding author.
E-mail address: annemie.vanhirtum@grenoble-inp.fr (A. Van Hirtum).

http://dx.doi.org/10.1016/j.apacoust.2015.11.019
0003-682X/

interaction somewhere in a duct has been show to be a simple way to fine-tune the associated auto-oscillation frequency and instability onset pressure [22] whereas other studies focus on the impact of the duct geometry on sound scattering for engine exhaust silencers [14].

In the following, the design and realization of the setup is detailed and characterized. Next, examples of quantitative measurements are discussed in order to provide evidence to what extent complex aero-acoustic phenomena, including transient regimes, can be produced, reproduced and hence studied. The impact of the duct geometry is shown.

2. Setup

2.1. Design

The design is inspired on recent work on the deformation of an a priori uniform circular (diameter $D = 2b_0$, with b_0 the radius of the undeformed circular cross-section) elastic duct by pinching it between two parallel bars [20]. A quasi-analytical geometrical model was proposed and validated to describe the pinched duct portion based firstly on the assumption of a constant perimeter ($P \simeq 2\pi b_0$) and secondly on the assumption that each cross-section can be described as a stadium ring. The internal shape of the duct is modeled as a function of the imposed pinching effort $\mathcal{P} = 1 - b_{x_c}/b_0$ with $b_{x_c} \leqslant b_0$ corresponding to the minimum radius of the compressed duct. The approach results in an characteristic error of less than 4% of the duct's diameter for pinching efforts between 40% and 95%. Besides the low computational cost, the quasi-analytical duct model has the advantage to depend on a single parameter b_{x_c} defining the imposed pinching effort at position x_c. Moreover, the model holds regardless the importance of the applied constriction effort $\mathcal{P}$ (small, modest or severe pinching efforts). A pinched circular duct of length L oriented along the x-direction is illustrated in Fig. 1(a). Main geometrical parameters are indicated: undeformed circular internal radius b_0 defining perimeter P, wall thickness d, pinching position x_c, major $a(x)$ and minor $b(x)$ axes of the cross-section.

The design of the setup exploits these features by aiming to control as a function of time t the position of pinching along the duct's main axis $x_c(t)$ as well as the pinching effort $\mathcal{P}$ by imposing $b_{x_c}(t)$. Consequently, the pinched duct's geometry can be approximated from the time-dependent parameter set $\{b_{x_c}, x_c\}(t)$ using the geometrical duct model following the flowchart indicated in Fig. 2 and its outcome is illustrated in Fig. 1(b). The instantaneous input parameter set $\{b_{x_c}, x_c\}$ consists of the constriction position (x_c) and the minor axis at this position (b_{x_c}). Besides time-varying parameters, two constant geometrical duct parameters are given – unpinched internal radius and duct's length $\{b_0, L\}$ – as well as the internal diameter and length $\{D_l, l\}$ of the attachment portion which geometry is determined by the way the duct is mounted to the remaining of the setup (see realization in Section 2.2). Therefore, the geometry is modeled for longitudinal x-positions in the range $-L + l < x \leqslant 0$.

Concretely, for a pincer consisting of two parallel round bars and a duct with internal radius b_0, the minor axis at each longitudinal position $b(x)$ at time instant t is then estimated from the known input parameters as [20]:

$$b_{(x_c,b_{x_c})}(x) = b_0 - b_0 \cdot \left(1 - \frac{b_{x_c}}{b_0}\right) \cdot \left(\frac{(x - x_c)^2}{\alpha_b^2} + 1\right)^{-1}, \tag{1}$$

with in the case of a pincer with parallel round bars of diameter 6.4 mm

$$\alpha_b(1 - \beta(x_c)) = 48 \cdot (1 - \beta(x_c))^2 - 70 \cdot (1 - \beta(x_c)) + 39, \tag{2}$$

$$\beta(x) = b(x)/b_0. \tag{3}$$

Once minor axis $b(x)$ is known at each longitudinal x-position, the corresponding duct's cross-section in polar coordinates (r, θ) is modeled as a piecewise function of $\theta \in [0, 2\pi]$:

$$r_b(\theta) = \begin{cases} \frac{b}{\sin(\theta)}, & \text{for } \varphi \leqslant \theta \leqslant \pi - \varphi, \\ \frac{\pi}{2} b \frac{1-\beta}{\beta} \left[\left(\frac{4}{\pi^2} \left(\frac{\beta}{1-\beta} \right)^2 - \sin^2(\theta) \right)^{1/2} + \cos(\theta) \right], & \text{for } -\varphi < \theta < \varphi, \\ \frac{\pi}{2} b \frac{1-\beta}{\beta} \left[\left(\frac{4}{\pi^2} \left(\frac{\beta}{1-\beta} \right)^2 - \sin^2(\theta) \right)^{1/2} - \cos(\theta) \right], & \text{for } \pi - \varphi < \theta < \pi + \varphi, \\ -\frac{b}{\sin(\theta)}, & \text{for } \pi + \varphi \leqslant \theta \leqslant 2\pi - \varphi, \end{cases} \tag{4}$$

with critical angle $\varphi(b) = \arctan \frac{2}{\pi} \frac{\beta}{1-\beta}$.

Other geometrical variables important for aero-acoustic applications such as the area function $A(x)$ or major axis $a(x)$ can then be expressed as a function of minor axis $b(x)$ as well:

$$A(x) = \pi b^2 + 2\pi b_0^2 \beta (1 - \beta), \tag{5}$$

$$a(x) = b + \frac{\pi}{2} b_0 (1 - \beta). \tag{6}$$

Following this design outlined in Fig. 2, the duct's geometry can be accurately modeled for a duct pinched between two parallel blocks with circular extrema of diameter 6.4 mm enveloping the duct in the plane perpendicular to the duct's longitudinal axis (x-direction) at a known constriction position x_c and for a known minor axis at this position b_{x_c}. Consequently, in the next Section 2.2

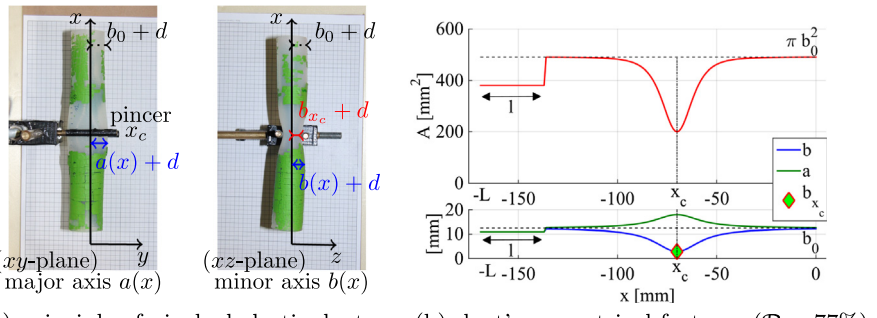

(a) principle of pinched elastic duct (b) duct's geometrical features ($\mathcal{P} = 77\%$)

Fig. 1. (a) Main parameters of a pinched duct (unpinched internal radius b_0 or constant perimeter $P \simeq 2\pi b_0$, constant wall thickness d) along the z-direction for pinching effort $\mathcal{P} = 1 - b_{x_c}/b_0$ applied at longitudinal position x_c. (b) Some modeled geometrical quantities (area $A(x)$, major $a(x)$ and minor $b(x)$) for a duct of length L for known input of constriction position x_c and imposed pinching effort $\mathcal{P}$ associated with b_{x_c}. The duct's exit is taken as the origin of the x-axis so that its inlet corresponds to $-L$. Attachment length l is indicated (length corresponding to connection of the duct to remaining of the setup (Section 2.2) for which the diameter is reduced to D_l).

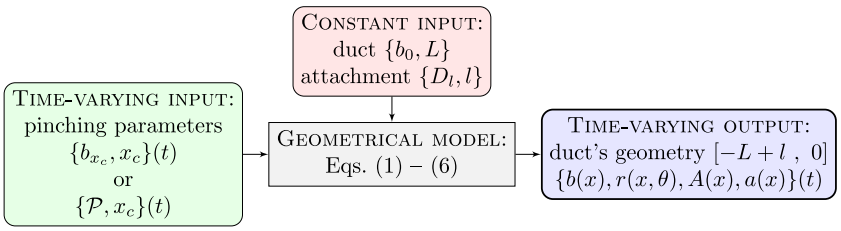

Fig. 2. Geometrical model flow chart for a single pincer indicating time-varying and constant input parameters as well as output variables (cross-section radius $r(x,\theta)$ with $0 \leqslant \theta \leqslant 2\pi$, area $A(x)$, major $a(x)$ and minor $b(x)$). Some of the output parameters are illustrated in Fig. 1(b).

the realization of a pincer is detailed as well as how input parameters (pinching effort $\mathcal{P}(t)$ and pinching position $x_c(t)$) relate to experimental setpoint parameters in order to prescribe the geometry as a function of time.

2.2. Realization

The realization of the setup for two pincers (indicated by subscript index i, the subscript is omitted in case a single pincer is used) is illustrated in Fig. 3. The realization aims to control experimental setpoints defining model input parameters $\{x_c(t), b_{x_c}(t)\}$ as well as to give feedback of their actual values as a function of time t. A duct of internal radius $b_0 = 12.5$ mm (or $D = 25$ mm), length $L = 171$ mm and wall thickness $d = 3$ mm is considered. The reduced diameter of the attachment portion of length $l = 33$ mm yields $D_l = 22$ mm.

2.2.1. Pinching effort setpoints and feedback: z direction – $\{\Delta z, V_z\}$

A pincer consists of two identical pincer blocks. Rapid prototyping (Ultimaker 2, 20 μm definition) is used to realize each pincer block as a rounded rectangular portion (height 23.2 mm and width 65 mm) for which the thickness corresponds to the diameter of the rounded ending of diameter 6.4 mm. The non-rounded rectangular edge is mounted to a linear actuator (step motor SMC LEYG16 with speed $V_z < 500$ mm/s and accuracy 0.02 mm/step) equipped with a gliding system with maximum stroke $\max(\Delta z) = 50$ mm. Each actuator is powered (Traco TCL-120) and controlled (SMC lecP6) independently in order to fully control the displacement of each actuator and hence pincer block in time (stroke Δz and speed V_z). The actuator is equipped with an integrated optical encoder enabling to track its stroke Δz and the sense of its movement along the z direction. Communication with the controller and the encoder is done using a multiple input and multiple output data acquisition card (PC/DAQ, National Instruments NI-PXIe-1073, NI-PXIe6363, NI-PXI-4330) and connector block (BNC-2090A) together with LabView (National Instruments).

The positioning of the pincer blocks with respect to the duct and actuators is depicted in Fig. 3. A single pincer is then composed of two pincer blocks (actuators) so that their combined maximum stroke yields $2 \times \max(\Delta z) = 100$ mm. The pinching effort $\mathcal{P}(t)$ at position x_c – or equivalently $b_{x_c}(t)$ since $\mathcal{P} = 1 - b_{x_c}(t)/b_0$ holds – is then controlled by imposing the stroke $2 \times \Delta z$ since both are related by a constant offset as shown in Fig. 4. The value of the offset is determined (see Fig. 4(a)) by imposing steady setpoints $0 < \Delta z < 50$ whose actual value is measured by the encoders. In addition, a caliper was used to measure $2(b_{x_c} + d)$ at the outside of the tube. The correction of $100 - 2\Delta z$ obtained from the measured encoder stroke values using a constant offset matches $2(b_{x_c} + d)$ measured with the caliper. Once the value of the offset is known (and wall thickness d), gathering of the time-varying encoder signal informs on the actual speed of variation V_z as well as on the magnitude of the pinching effort b_{x_c} as a function of time t. This is illustrated in Fig. 4(b). Since wall thickness d is supposed constant, the ratio of the pinching effort $\mathcal{P}$ based on b_{x_c} (internal duct's minor axis) and the external pinching effort $\mathcal{P}_{ext}$ based on $b_{x_c} + d$ (external duct's minor axis) is constant as well and yields $\mathcal{P}/\mathcal{P}_{ext} = 1 + b_0/d$ as shown in Fig. 5 for the case of internal diameter $D = 25$ mm and wall thickness $d = 3$ mm.

2.2.2. Pinching position setpoints and feedback: x direction – $\{\Delta x, V_x\}$

In order to control the longitudinal x-position of a pincer at each time instant $x_c(t)$ each pincher is mounted to a one-dimensional positioning system (IGUS SHT-12-AWM-500, step motor Sanyo Denki 103h5208 with accuracy 0.01 mm/step and speed $V_x < 500$ steps/s) with maximal stroke of $\max(\Delta x) = 500$ mm and which is controlled using an Arduino Uno board with motor-shield. Communication with the Arduino board is done using labView in order to set the extent Δx ($0 < \Delta x < L - l$ in the case $L - l < \max(\Delta z)$) of the longitudinal displacement of the pincer as well as its velocity setpoint $V_x < 500$ steps/s. The actual speed V_x is determined as the ratio of the displacement extent and the duration of the displacement measured with the Arduino board.

3. Characterisation of the setup

3.1. Time-varying pinching effort and position: setpoints versus feedback

3.1.1. Pinching effort setpoints versus feedback: z direction

The relationship between setpoints and measured pincer V_z velocities [mm/s] is characterized as a function of the extent of displacement Δz. Fig. 6 compares setpoints and measured V_z velocities for $\Delta z = 10$ mm and $\Delta z = 50$ mm (corresponding to the maximum displacement stroke). Setpoints and measured V_z velocities match within 10% as the value of the setpoint velocity is increased from 10 mm/s until the measured velocity saturates. The setpoint corresponding to saturation decreases with the displacement extent Δz, *e.g.* up to $V_z \simeq 250$ mm/s for $\Delta z = 10$ mm and up to $V_z \simeq 350$ mm/s for $\Delta z = 50$ mm. From Fig. 6 is further seen that the repeatability is excellent (<5%) except for the most extreme combination (Δz =50 mm and setpoint velocity $V_z = 500$ mm/s).

3.1.2. Pinching position setpoints versus feedback: x direction

Given the length of the duct's deformable portion ($L - l \approx 135$ mm see Fig. 3) in the realized setup longitudinal displacements Δx of the pincers along the x-direction in a range up to 80 mm were characterized so that no deformation occurs near the inlet (of the deformable portion) or exit. The relation between setpoint velocities V_x [steps/s] and measured velocities V_x [mm/s] is characterized for different displacement extents Δx [mm] as reported in Fig. 7. Note that shown setpoints of 150, 300, 500 and 700 steps/s correspond to 1.5, 3, 5 and 7 mm/s, respectively given the resolution of 0.01 mm/step. At first, *i.e.* as the extent is increased from zero, measured V_x velocities increases with the displacement extent Δx until saturation occurs at $\max(V_x)$ (see left

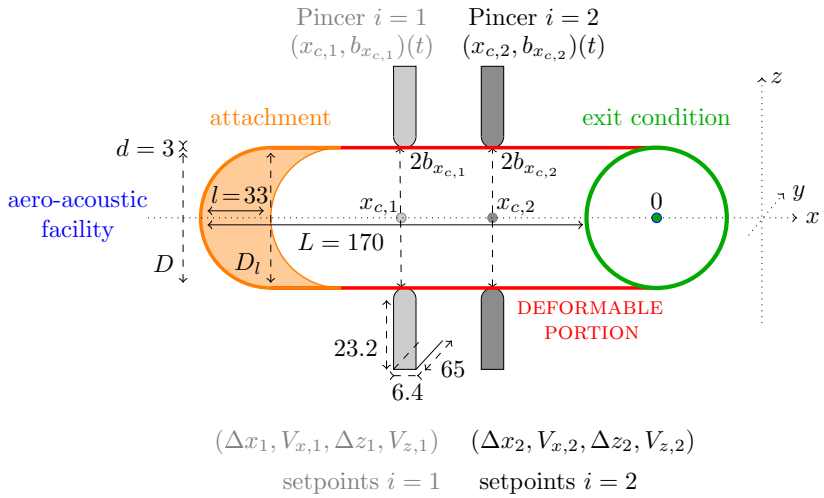

(a) overview time-varying geometrical model parameters and discrete setup setpoints

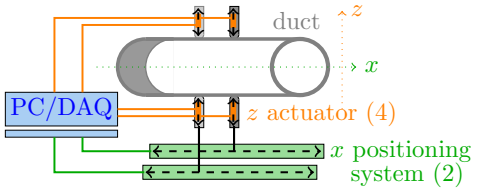

(b) overview setup elements used for setpoint control

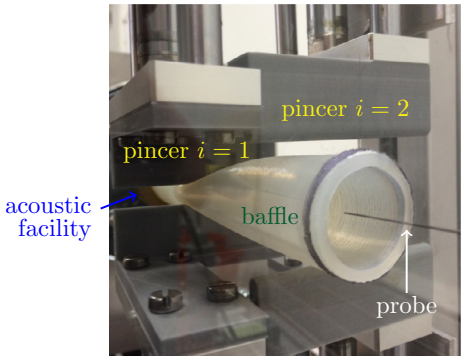

(c) probe

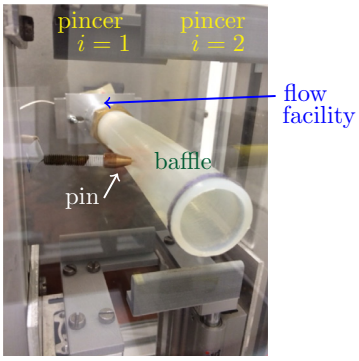

(d) pin

Fig. 3. Illustration of the realization of a deformable duct with two pincers (subscript i) whose positions along the x-direction (pinching parameter $x_{c,i}(t)$) and along the z-direction (pinching parameter $b_{x_{c,i}}(t)$ are controlled independently): (a) overview of pinching parameters and main dimensions [mm], (b) overview of setup elements used for setpoint control, (c,d) photographs of duct with rigid flat transparent baffle (exit condition) with sensor placement (microphone probe or moveable pin with pressure transducer).

side of Fig. 7). For $\Delta x > 20$ mm the measured V_x velocity is within 10% of its saturation value regardless of the setpoint velocity (shaded areas in Fig. 7). The saturation value $\max(V_x)$ [mm/s] (for $\Delta x > 20$ mm) can be described as quadratic for setpoint velocities $V_x \leq 500$ steps/s and constant (measured velocity $V_x \simeq 3.3$ mm/s) for setpoint velocities $V_x > 500$ steps/s. In the following, experiments are performed for setpoint velocity $V_x = 300$ steps/s so that for $\Delta x > 10$ mm, the measured speed is within 10% of its measured saturation value $\max(V_x) = 2.5$ mm/s so that a displacement $\Delta x = 40$ mm takes 16 s.

3.2. Noise inherent to the setup

Some noise is generated by the computer controlled motor-driven variation of pinching effort (along the z-direction) or pinching position (along the x-direction). Features of the measured noise (microphone B&K 2669L and preconditioner B&K 5935L, sampling frequency 50,000 Hz) are analyzed in order to assess the potential impact on acoustic experiments.

Measured SPL level yields 67 dB SPL for a displacement along z-direction which is of the same order of magnitude as measured for PC use (68 dB SPL [21]) in the same environment which represents the reference level of background noise. Measured SPL level yields 76 dB SPL for a displacement along longitudinal x-direction which is an increase compared to the reference level, but still limited compared to the noise associated with typical environmental noise sources used during aero-acoustic experiments such as the use of the flow facility (about 90 dB SPL [21]) described in Section 4. Consequently, the measured noise levels are low compared to levels expected during aero-acoustic experiments.

Next, spectral noise features are assessed. A typical normalized power spectrum for a displacement of a pincer along the z-direction is shown in Fig. 8. Narrow spectral peaks are observed at 10 kHz and 20 kHz. These peaks characterize spectra associated

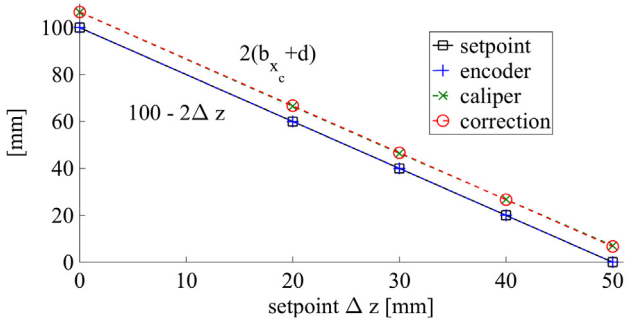

(a) steady, constant setpoints Δz

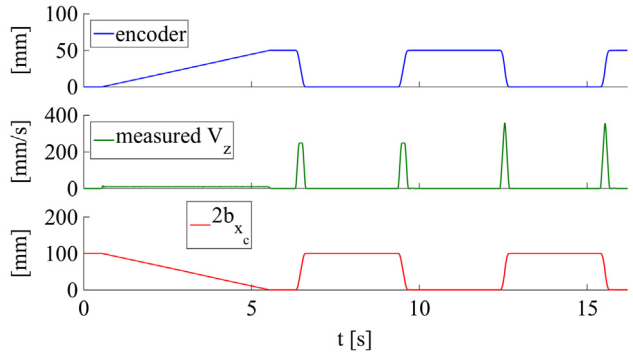

(b) unsteady, time-varying setpoints Δz

Fig. 4. Illustration of relationship between (a) imposed setpoint Δz and resulting values of $100 - 2\Delta(z)$ measured encoder signal, estimated values of $2(b_{x_c} + d)$ and validation using a caliper. (b) Measured encoder signal and corresponding values of speed V_z and $2b_{x_c}$ as a function of time t.

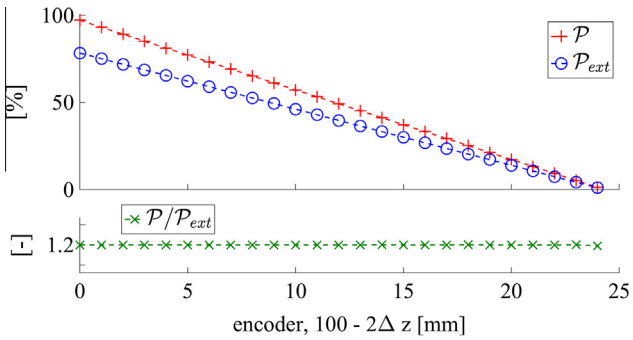

Fig. 5. Pinching efforts for a duct with internal diameter $D = 25$ mm and wall thickness $d = 3$ mm as a function of $100 - 2\Delta z$ measured by the encoder: (a) $\mathcal{P}$ based on the duct's internal minor axis b_{x_c} as defined in Section 2.1 and $\mathcal{P}_{ext}$ based on the duct's external minor axis $b_{x_c} + d$. (b) Ratio of $\mathcal{P}$ and $\mathcal{P}_{ext}$.

with a displacement of a pincer along the x-direction as well. Consequently, the impact of the displacement on the spectral content is limited to well identified frequencies (10 kHz and 20 kHz).

4. Aero-acoustic facility: experiments without and with flow supply

In order to illustrate the use of the realized setup for aero-acoustic studies involving ducts with time-varying geometry (and hence to illustrate the impact of the setpoint parameters described in Section 2.2) the setup is mounted to an aero-acoustic facility as depicted in Fig. 3. As outlined in the introduction, acoustic sources of different nature are encountered in physiological applications. Therefore, two aero-acoustic facilities

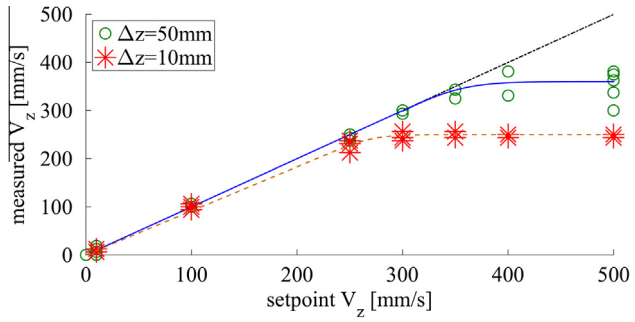

Fig. 6. Velocity V_z (setpoint [mm/s] and measured [mm/s]) for displacement extents $\Delta z = 10$ mm (☆) and $\Delta z = 50$ mm (○). Matching (dashed line) and tendencies (full and dash-dot lines).

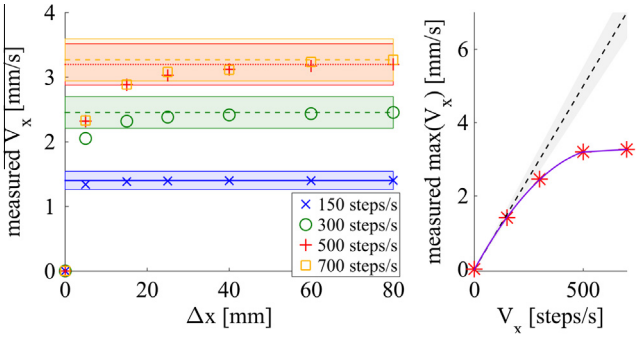

Fig. 7. Velocity V_x (setpoint [steps/s] and measured [mm/s] as a function of displacement extents Δx. (Left) For each setpoint velocity the shaded area indicates the range of the maximum value (horizontal line) plus-minus 10% ($\max(V_x) \pm 10\%$). (Right) The relationship between setpoint velocities and measured maximum values $\max(V_x)$ [mm/s] (☆). Matching (dashed line) and tendencies (full line) are indicated.

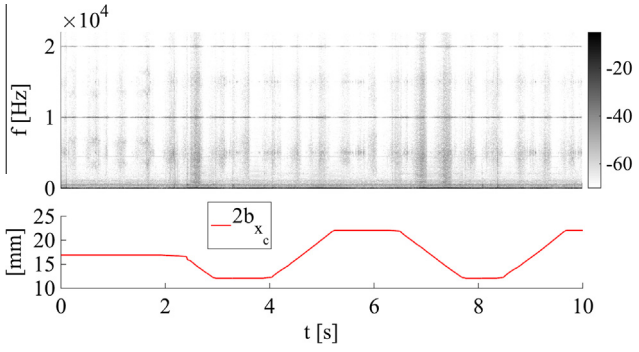

Fig. 8. Example of normalized power spectrum [dB] (top) of noise generated during variation of pinching effort ($2b_{x_c}$ [mm]) as a function of time t [s] (bottom).

are described in the following allowing experiments without (acoustic facility, Section 4.1) and with flow supply (flow facility, Section 4.2). The duct's exit was fixed in a rigid flat transparent baffle (37 cm × 35 cm and thickness 5 mm, see Fig. 3(c)) positioned parallel with the duct's exit (the chosen exit condition is *e.g.* of interest to mimic a face when phenomena related to the upper airway are studied) so that a single exit condition is considered. Obviously, different exit conditions can be assessed to mimic different flow nozzles or acoustic radiation conditions. The multiple input and multiple output data acquisition card described in Section 2.2 is used during all measurements to capture sensor data or generate signals.

4.1. Acoustic facility

To perform acoustic experiments without flow, the deformable duct was attached to an acoustic source facility (sinusoidal and white noise signals generated by a compression chamber (Monacor KU-916T) for frequency range from 0.1–4 kHz) by means of a rigid connecting piece with central communication hole of diameter 2 mm. Acoustic pressure $p(t)$ was measured at a fixed position inside the duct along its centerline ($x = -12$ mm, $z = 0$ mm) using an acoustic probe (UA 9005, diameter 1 mm and length 200 mm) attached to a microphone (microphone B&K 2669L and preconditioner B&K 5935L). The probe's position is illustrated in Fig. 3(c).

4.2. Flow facility

To perform aero-acoustic experiments with flow, the deformable duct was attached to a flow facility with settling box. The flow facility consisted of an air compressor (Atlas Copco GA7 isolated in a separated room), followed by a pressure regulator (Norgren type 11-818-987) and a manual valve so that the volume flow rate Q was controlled (4043 TSI). The replica was mounted to an upstream settling box ($0.25\,\text{m} \times 0.3\,\text{m} \times 0.35\,\text{m}$) tapered with acoustic foam (SE50-AL-ML Elastomeres Solutions) and equipped with flow straighteners in order to avoid acoustic resonances (due to the flow facility setup or settling chamber) and to homogenize the flow. Downstream the settling chamber, a uniform rigid round extension duct of diameter $\varnothing = 25$ mm (same diameter as the deformable duct) with streamwise (x-direction) length $L_u = 2$ cm is placed followed by a rigid clamping piece with internal diameter $\varnothing = 25$ mm and length 1.5 cm to which a rigid round downstream duct (diameter $\varnothing = 25$ mm, length $L_d = 6$ cm) is attached in order to mount the deformable duct. The clamping piece contains a stretched membrane (latex sheet of thickness 0.2 mm, Piercan Ltd) which was slit (center cut of 12 mm) so that air could pass through it. A strong acoustic source is generated due to fluid–structure interaction when auto-oscillation of the membrane occurs [23]. Additionally, sound is generated aerodynamically downstream of the membrane when air passes through the duct.

A pressure transducer (Kulite XCS-093) was placed in a fixed pressure tap (diameter 0.4 mm) immediately upstream from the membrane in order to measure the upstream pressure $P_u(t)$. The pressure downstream from the membrane inside the deformable duct $P_d(t)$ is measured by placing a pressure sensor into a pressure tap (diameter 0.4 mm) which can be pinned in the duct's wall. Concretely, the pin is placed at $x = -65$ mm as shown in Fig. 3(d).

5. Experimental evidence for influence of pinching

Experiments are performed in order to illustrate the influence of the pinching by considering $\{\mathcal{P}, V_z, x_c, V_x\}$ describing the time-varying geometry of the deformable portion of the duct. In the

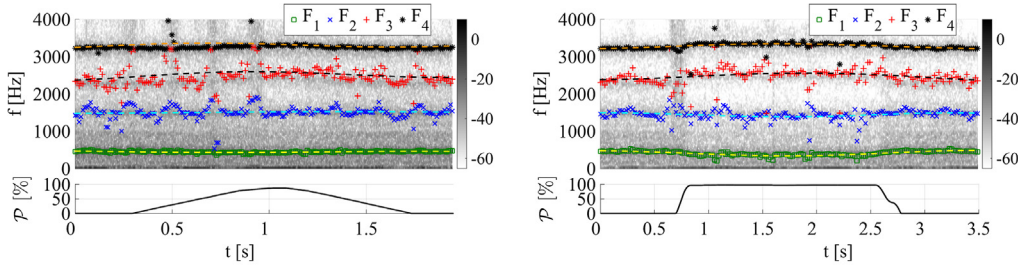

(a) $x_c = -26$mm: $V_z = 10$mm/s (left) and $V_z = 200$mm/s (right)

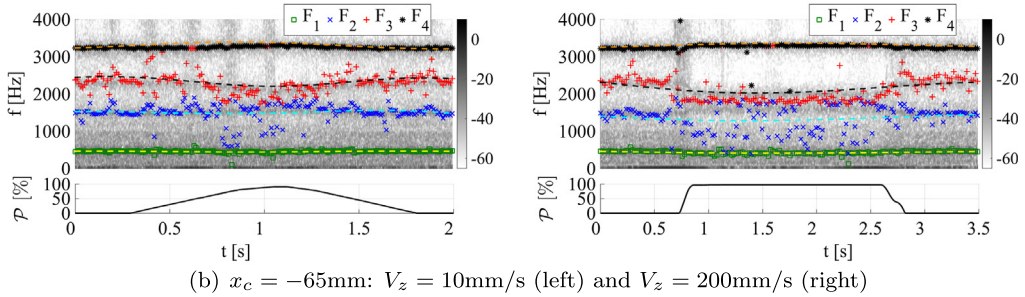

(b) $x_c = -65$mm: $V_z = 10$mm/s (left) and $V_z = 200$mm/s (right)

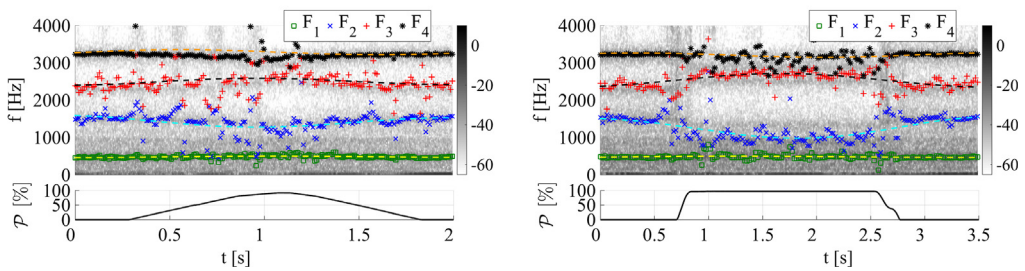

(c) $x_c = -105$mm: $V_z = 10$mm/s (left) and $V_z = 200$mm/s (right)

Fig. 9. Illustration of acoustic pressure spectrograms as a function of time t for setpoints $0 \leqslant \mathcal{P} \leqslant 97\%$ and $V_z \in \{10,\ 200\}$ mm/s for different pinching positions x_c. Resonances F_1 (○), F_2 (×), F_3 (+) and F_4 (★) are depicted for: (a) $x_c = -26$ mm, (b) $x_c = -65$ mm and (c) $x_c = -105$ mm.

following, typical examples are given for the setup (Fig. 3) mounted to the acoustic facility (Section 5.1) and to the flow facility (Section 5.2), respectively.

5.1. Acoustic facility: influence of $\mathcal{P}, V_z, x_c$ and V_x

White noise excitation is applied at the inlet of the deformable tube using the acoustic facility described in Section 4.1 in order to investigate the impact of the different setpoints on acoustic duct resonances [9,10,17] by considering the spectrogram of the acoustic pressure $p(t)$. Resonances are manually checked as well as extracted applying established signal processing techniques based on linear predictive coding [9,10,17].

Fig. 9 illustrates characteristic spectrograms for a variation of the pinching effort ($0 \leqslant \mathcal{P} \leqslant 97\%$) at different rates ($V_z \in \{10, 200\}$ mm/s) and at different pinching positions ($x_c \in \{-26, -65, -105\}$ mm). For pinching efforts $\mathcal{P} < 50\%$ spectra are determined by odd multiples of the first resonance at $F_1 \approx 475$ Hz as expected for a half open duct regardless of pinching position x_c [17,4]. For pinching efforts $\mathcal{P} > 50\%$ resonances shift as a function of the pinching effort $\mathcal{P}$. Moreover, the shift depends on the pinching position x_c as well. Indeed from Fig. 9 is seen that increasing the pinching effort from $\mathcal{P} = 0\%$ to $\mathcal{P} = 97\%$ increases resonance F_3 for $x_c = -105$ mm ($F_3 \approx 2700$ Hz) and for $x_c = -26$ mm ($F_3 \approx 2450$ Hz) whereas the resonance decreases for $x_c = -65$ mm ($F_3 \approx 1900$ Hz). In general, it is observed that the resonance frequency shift is larger for F_2 and F_3 than for F_1 and F_4. The impact of the rate of variation of the pinching effort V_z is marginal, so that as a first approximation the variation of pinching effort $\mathcal{P}$ can be considered quasi-steady. Note however, that the performance of the automated resonance detection algorithm deteriorates as the duration of the transient time associated with $\mathcal{P}$ variation decreases, *i.e.* as V_z increases, as well as when resonance values become close (*e.g.* detection of F_2 fails for $\mathcal{P} = 97\%$ at $x_c = -65$ mm and $V_z = 200$ mm/s as seen in Fig. 9).

Fig. 10 further highlights the influence of varying pinching position $-105 \leqslant x_c \leqslant -25$ mm for a constant pinching effort ($\mathcal{P}$ set to 57% and 97%, respectively in Fig. 10(a)) as well as for a variation of pinching effort ($0 \leqslant \mathcal{P} \leqslant 97\%$ in Fig. 10(b)). It is seen from Fig. 10(b) (right) that resonance frequencies (in particular F_2 and

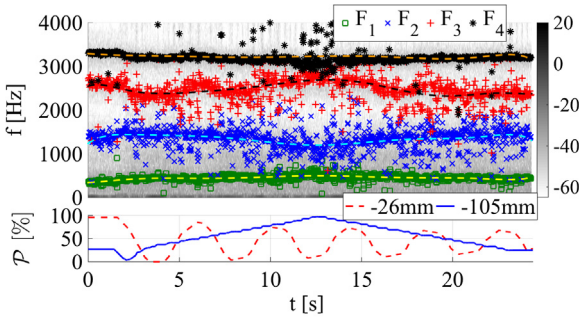

(a) $x_{c,1} = -26$mm and $x_{c,2} = -105$mm

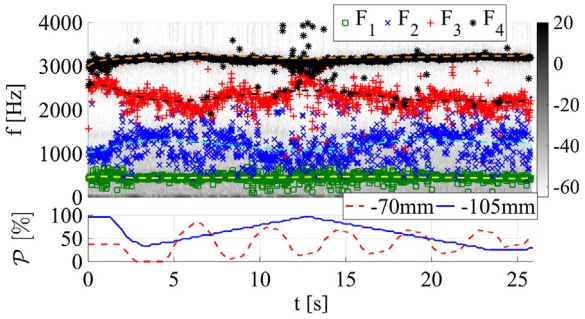

(b) $x_{c,1} = -70$mm and $x_{c,2} = -105$mm

Fig. 11. Illustration of acoustic pressure spectrograms as a function of time t for setpoints $0 \leqslant \mathcal{P} \leqslant 97\%$ and $V_z = 50$ mm/s for pinching efforts imposed at two pinching positions simultaneously, *i.e.* $x_{c,1}$ and $x_{c,2}$ as depicted in Fig. 3. Resonances F_1 (○), F_2 (×), F_3 (+) and F_4 (★) are depicted for: (a) $x_{c,1} = -26$ mm and $x_{c,2} = -105$ mm and (b) $x_{c,1} = -70$ mm and $x_{c,2} = -105$ mm.

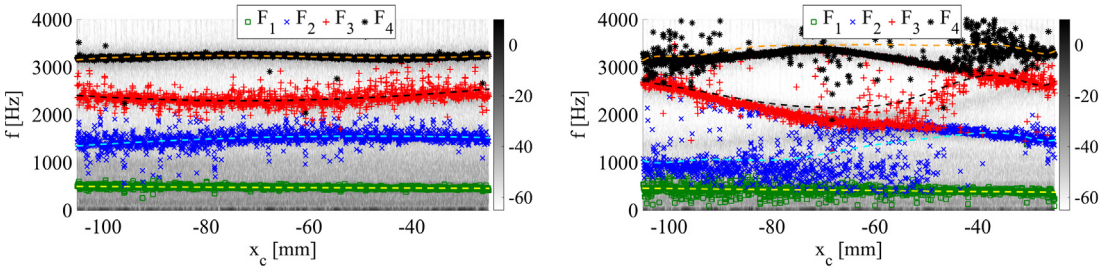

(a) constant pinching effort: $\mathcal{P} = 57\%$ (left) and $\mathcal{P} = 97\%$ (right)

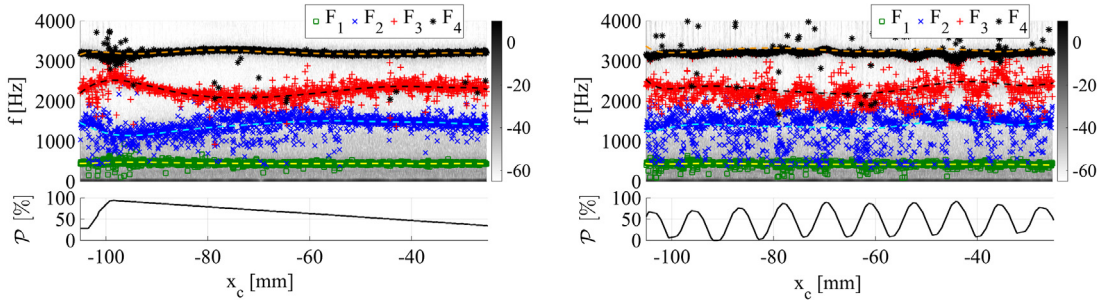

(b) varying pinching effort: $0 \leq \mathcal{P} \leq 97\%$

Fig. 10. Illustration of acoustic pressure spectrograms as a function of pinching position $-105 \leqslant x_c \leqslant -25$ mm at velocity $V_x = 2.5$ mm/s. Resonances F_1 (○), F_2 (×), F_3 (+) and F_4 (★) are depicted for: a) constant pinching effort $\mathcal{P} = 57\%$ (left) and $\mathcal{P} = 97\%$ (right) and b) varying pinching effort in the range $0 \leqslant \mathcal{P} \leqslant 97\%$ at velocity $V_z = 50$ mm/s.

F_3) are very sensitive to variation of both pinching position and pinching effort in the range $0 \leqslant \mathcal{P} \leqslant 97\%$.

Fig. 11 shows that for rapid variation of the pinching effort $\mathcal{P}$ at one pinching position ($x_{c,2} = -105$ mm in Fig. 11) the resonance frequencies can be tuned also by imposing a pinching effort at a second pinching position ($x_{c,1} = -26$ mm and $x_{c,1} = -105$ mm in Fig. 11). Indeed, from Fig. 11 is easily observed that *e.g.* the frequency spacing between F_3 and F_4 is enlarged when the additional pincer is positioned at $x_{c,1} = -70$ mm compared to position $x_{c,1} = -26$ mm.

The duct's response to white noise excitation shows that several strategies can be applied to vary acoustic duct resonances by varying pinching position and pinching degree for a single pincher as well as by using two pinchers. The duct's response to a particular frequency using a sinusoidal excitation signal with known frequency is illustrated for $f_0 = 3250$ Hz at pinching position $x_c = -26$ mm and $f_0 = 1650$ Hz at pinching position $x_c = -70$ mm in Fig. 12. The repetition of the variation of pinching degree in the range $0 \leqslant \mathcal{P} \leqslant 97\%$, increasing as well as decreasing, is observed not to alter the associated magnitude and pressure of the measured acoustic pressure. The frequency response is further illustrated in Fig. 13. The magnitude and phase of the acoustic pressure as a function of pinching effort $\mathcal{P}$ are compared for different frequencies ($f_0 < 4$ kHz) at pinching position ($x_c = -70$ Hz) in Fig. 13(a). It is seen that a pronounced maximum in acoustic pressure occurs for 2200 Hz at pinching degree $\mathcal{P} \approx 65\%$ and for 3250 Hz at a large pinching effort $\mathcal{P} \approx 90\%$ and the phase varies in accordance. For lower frequencies ($f_0 = 1075$ Hz and $f_0 - 1650$ Hz) the magnitude and phase is rather flat so that their values are almost not affected by the tube's geometry, *i.e.* pinching effort $\mathcal{P}$. To further illustrate the impact of the tube's geometry on the magnitude and phase of the acoustic pressure, Fig. 13(b) illustrates their values when besides the pinching effort ($0 \leqslant \mathcal{P} \leqslant 95\%$) also the pinching position ($-105 \leqslant x_c \leqslant -26$ mm) is changed while the sinusoidal excitation frequency ($f_0 = 2200$ Hz) is held constant. The position of the maximum magnitude response is observed to shift with the pinching position.

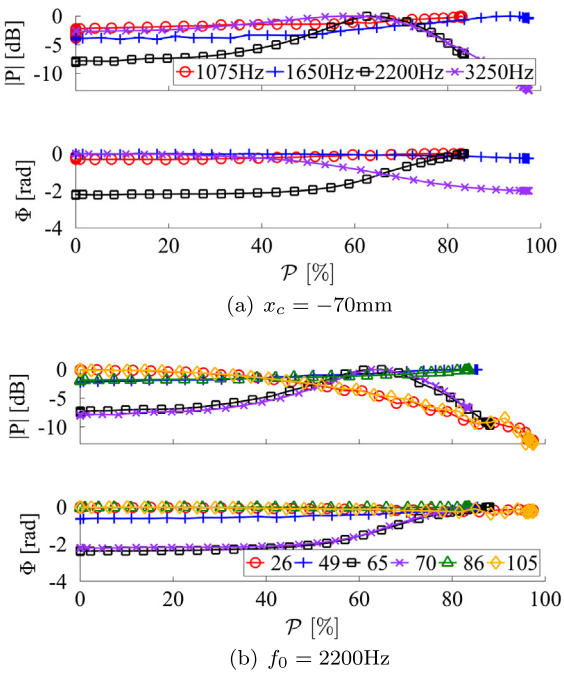

Fig. 13. Illustration of normalized amplitude P [dB] and phase Φ [rad] of acoustic pressure $p(t)$ as a function of pinching effort $0 \leqslant \mathcal{P} \leqslant 97\%$ and $V_z = 50$ mm/s. (a) $f_0 < 4$ kHz at pinching position $x_c = -70$ mm and (b) $f_0 = 2200$ Hz at pinching positions $-105 \leqslant x_c \leqslant -26$ mm.

5.2. Flow facility: influence of $\mathcal{P}$ and x_c

Experiments using the flow facility are illustrated in Fig. 14 for different pinching efforts applied at two pinching positions $x_{c,1} = -93$ mm and $x_{c,2} = -26$ mm, respectively. For a uniform tube ($\mathcal{P} = 0$ in Fig. 14(a) (left)) increasing upstream pressure P_u induces auto-oscillation of the membrane and subsequent decreasing the upstream pressure ceases oscillation. During auto-oscillation the spectrogram of the pressure within the tube P_d exhibits a harmonic contents which is determined by the oscillation frequency of the membrane. Depending on the pinching position, auto-oscillation of the membrane either stops or continues, as observed when comparing pressure signals at $x_c = -26$ mm for which oscillation stops (Fig. 14(b) (left)) and $x_c = -93$ mm for which oscillation continues (Fig. 14(b) (right)). Besides determining the onset and offset of the oscillation, the pinching position also alters the spectral content (see Fig. 14(b) (right)) by altering the oscillation frequency and

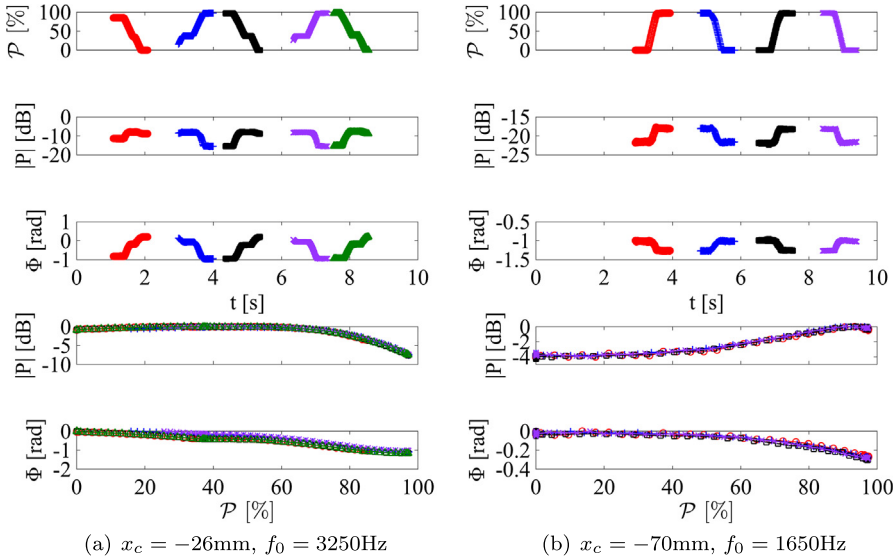

Fig. 12. Illustration of normalized amplitude P [dB] and phase Φ [rad] of acoustic pressure $p(t)$ as a function of time t [s] for repeated setpoints $0 \leqslant \mathcal{P} \leqslant 97\%$ and $V_z = 50$ mm/s. The magnitude and phase are expressed as a function of pinching effort as well: (a) $x_c = -26$ mm and $f_0 = 3250$ Hz and (b) $x_c = -70$ mm and $f_0 = 1650$ Hz.

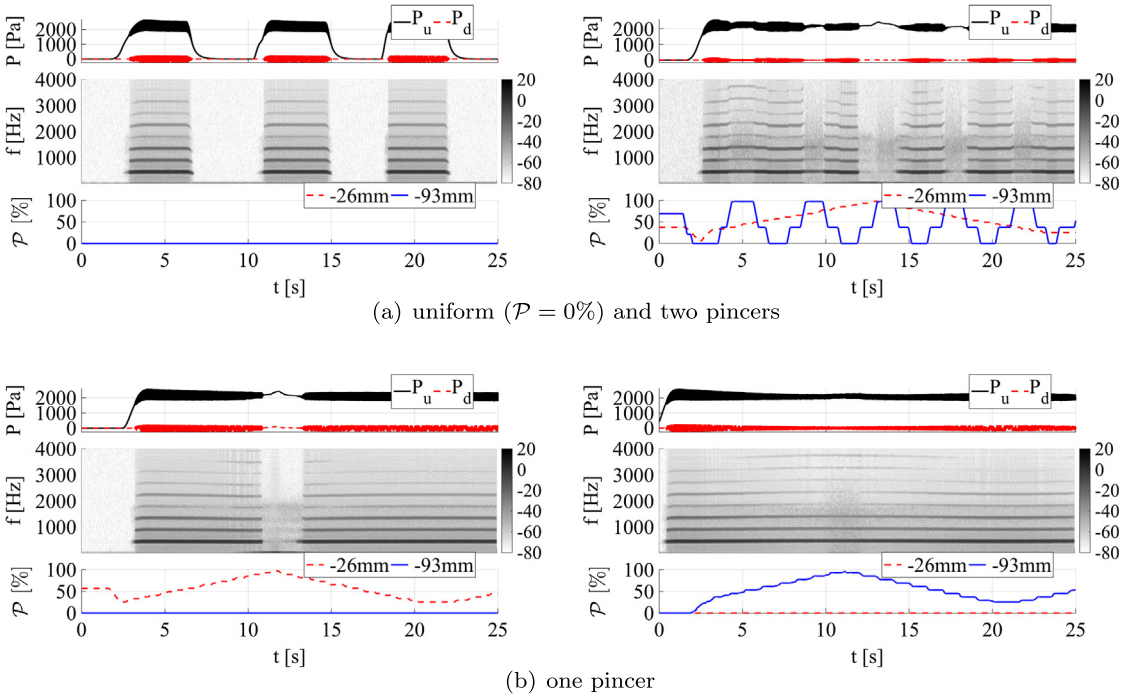

Fig. 14. Illustration of air pressure measured upstream from the membrane P_u [Pa] and within the tube P_d [Pa] and associated spectrogram of P_d [dB] as a function of time t [s] for different combinations of pinching efforts $\mathcal{P}$ at pinching position $x_{c,1} = -93$ mm and $x_{c,2} = -26$ mm, respectively.

the amplitude of the harmonics. This is further illustrated by applying pinching at both $x_{c,1} = -93$ mm and $x_{c,2} = -26$ mm (Fig. 14(a) (right)). Indeed, the value of the oscillation frequency and associated harmonics increases as the pinching effort is increased at $x_c = -93$ mm whereas oscillation stops when the pinching effort is increased at $x_c = -26$ mm. Consequently, varying the pinching position and effort provides a strategy to alter observed oscillation features.

6. Discussion and conclusion

A setup is presented for which the setpoints ($\{\Delta x, V_x, \Delta z, V_z\}$) allow to control the variation of pinching positions ($x_c(t)$) and efforts ($\mathcal{P}(t)$) along a deformable tube pinched between two parallel bars. Using these input parameters ($x_c, \mathcal{P}$), the varying tube's geometry can be accurately estimated using a quasi-analytical geometrical model [20]. Since the geometry can be estimated as a function of time-varying setpoints of the control parameters, measurements using the setup can be used to characterize phenomena as well as to compare experimental observations with data obtained from numerical simulations. In addition, the limited number of input parameters – both experimentally as required for the quasi-analytical geometrical model – encourage comparison of experimental observations with analytical model results as well. Moreover, when aiming physiological applications the chosen set of input parameters is particularly interesting since they have not only a clear physiological meaning (constriction degree, duration, position), but their order of magnitude can be determined on human subjects either using expensive imaging techniques such as Magnetic Resonance Imaging (MRI) scans or X-ray computed tomography (CT) scans or yet relying on alternative measurement techniques such as pressure-flow measurements in case the upper airway geometry is of interest [24,11]. Moreover, it is noted that the use of a deformable tube and external pinching mechanisms avoids sharp edges. This feature might be of particular importance in order to avoid spurious aero-acoustic data since sharp edges are likely to cause unintended flow (*i.e.* flow separation or vortex shedding) and acoustic (*e.g.* sound generation and radiation) phenomena. Finally, it is noted that different geometrical features of the deformed portion, such as cross-section shape or extent, can be assessed by mounting pincer blocks with a different shape whereas the setup can be extended to involve more than two pincers if needed.

Examples of data obtained by mounting the setup equipped with two pincers to an aero-acoustic facility are shown. It was observed that varying pinching effort $\mathcal{P}$ and pinching position x_c alters the tube's acoustic resonances (acoustic facility) as well as the ongoing fluid–structure interaction (flow facility). A striking example of the influence of the constriction position x_c is provided by the shown experiments using the flow facility where for the same pinching effort $\mathcal{P} \approx 97\%$ the oscillation of the membrane is observed to be either inhibited ($x_c = -26$ mm) or to continue with a shifted oscillation frequency and altered spectral contents ($x_c = -93$ mm). In addition, examples of data using the acoustic facility show that different strategies can be used to vary the tube's resonances (F_2 and F_3 in particular). Consequently, the setup allows an accurate validation of experimental findings as a function of constant as well as time-varying tube's geometry's. Therefore, the current setup allows to study transient phenomena associated with variation of setpoints as well as with the variation of other control parameters used in the aero-acoustic facility such as the imposed upstream pressure when the flow facility is used. In addition, control strategies of acoustic resonances and auto-oscillation frequencies can be developed using the proposed setup.

Characterization of the current setup shows that the pinching effort can be accurately varied in the range $0 \leqslant \mathcal{P} \leqslant 100\%$ at a speed limited by its saturation value so that $V_z < 300$ mm/s. The same way the pinching position can be varied along the deformable portion $-L + l < x_c < 0$ whereas the speed of variation of the pinching position is again limited by its saturation value so that $V_x < 3.5$ mm/s. Therefore, it is evident that for applications needing a more rapid variation of either pinching effort (V_z) or pinching position (V_x) the setup can be improved in order to avoid or

increase values for which saturation occurs. In addition, a flat baffle was used as an exit condition in the current setup, it is clear that the impact of different exit conditions can be assessed as well as the impact of the tube length *L*.

Acknowledgments

This work was partly supported by EU-FET grant (EUNISON 308874). Martin Paour is acknowledged for his contribution to the experiments.

References

[1] Aalto D, Aaltonen O, Happonen RP, Jääsaari P, Kivelä A, Kuortti J, et al. Large scale data acquisition of simultaneous MRI and speech. Appl Acoust 2014;83:64–75.
[2] Bates JHT. Lumg mechanics. Cambridge, UK: Cambridge University Press; 2009.
[3] Bertram CD, Raymond CJ, Butcher KSA. Oscillations in a collapsed-tube analog of the brachial artery under a sphygmomanometer cuff. J Biomech Eng 1989;111:185–91.
[4] Blackstock DT. Fundamentals of physical acoustics. New York, USA: John Wiley & Sons; 2000.
[5] Boucher N, Prystupa A, Witczak A, Walczak E, Dzida G, Panasiuk L. Lung auscultation – identifcation of common lung sound abnormalities and associated pathologies. J Pre-Clin Clin Res 2013;7:32–5.
[6] Boyd JWR, Varley J. The uses of passive measurement of acoustic emissions from chemical engineering processes. Chem Eng Sci 2001;56:1749–67.
[7] Decramer M, Janssens W, Miravitlles M. Chronic obstructive pulmonary disease. Lancet 2012;379:1341–51.
[8] Drzewiecki GM, Melbin J, Noordergraaf A. The Krotkoff sound. Ann Biomed Eng 1989;17:325–59.
[9] Fant G. Acoustic theory of speech production. The Hague, The Netherlands: De Gruyter Mouton; 1971.
[10] Fletcher NH, Rossing TD. The physics of musical instruments. New York, USA: Springer-Verlag; 1998.
[11] Fujiso Y, Nozaki K, Van Hirtum A. Estimation of minimum oral tract constriction area in sibilant fricatives from aerodynamic data. J Acoust Soc Am 2015;138:EL20–5.
[12] Fung YC. Biomechanics circulation. New York, USA: Springer-Verlag; 1990.
[13] Gracco VL. Analysis of speech movements: practical considerations and clinical application. Technical report, Haskins Laboratories Status Report on Speech Research; 1997.
[14] Kooijman G, Hirschberg A, Auregan Y. Influence of mean flow profile and geometrical ratios on scattering of sound at a sudden area expansion in a duct. J Sound Vib 2010;39:607–26.
[15] Morse PM, Ingard KU. Theoretical acoustics. New York, USA: McGraw-Hill; 1987.
[16] Nu DN. Blood flow in arteries. Annu Rev Fluid Mech 1997;29:399–434.
[17] Pierce A. Acoustics, an introduction to its physical principles and applications. New York: Acoustical Society of America; 1991.
[18] Popescu M, Johansen ST, Shyy W. Flow-induced acoustics in corrugated pipes. Commun Comput Phys 2011;10:120–39.
[19] Story BH, Titze IR, Hoffman EA. Vocal tract area functions from magnetic resonance imaging. J Acoust Soc Am 1996;100:537–54.
[20] Van Hirtum A. Deformation of a circular elastic tube between two parallel bars: quasi-analytical geometrical ring models. Math Probl Eng 2015;2015:1–15.
[21] Van Hirtum A, Fujiso Y. Insulation room for aero-acoustic experiments at moderate Reynolds and low Mach numbers. Appl Acoust 2012;73:72–7.
[22] Van Hirtum A, Pelorson X. Modeling and validation of auto-oscillation onset in a constricted tube with application to phonation. J Fluids Struct 2015;58:40–8.
[23] von Helmholtz H. On the sensations of tone as a physiological basis for the theory of music. London, UK: Longmans, Green, and Co.; 1895.
[24] Warren D, DuBois A. A pressure-flow technique for measuring velopharyngeal orifice area during continuous speech. Cleft Palate J 1964;1:52–71.